Supplemental Material for "Simulating Holographic Conformal Field Theories on Hyperbolic Lattices"

Santanu Dey [1,2,*] Anffany Chen [1,2,†] Pablo Basteiro,[3,4] Alexander Fritzsche,[3,4,5] Martin Greiter [3,4]
Matthias Kaminski [6] Patrick M. Lenggenhager [4,7,8,9,10] René Meyer [3,4] Riccardo Sorbello,[3,4]
Alexander Stegmaier [3,4] Ronny Thomale [3,4] Johanna Erdmenger [3,4] and Igor Boettcher [1,2]

[1]*Department of Physics, University of Alberta, Edmonton, Alberta T6G 2E1, Canada*
[2]*Theoretical Physics Institute, University of Alberta, Edmonton, Alberta T6G 2E1, Canada*
[3]*Institute for Theoretical Physics and Astrophysics,*
Julius Maximilians University Würzburg, Am Hubland, 97074 Würzburg, Germany
[4]*Würzburg-Dresden Excellence Cluster ct.qmat, Julius Maximilians*
University Würzburg, Am Hubland, 97074 Würzburg, Germany
[5]*Institut für Physik, Universität Rostock, 18059 Rostock, Germany*
[6]*Department of Physics and Astronomy, University of Alabama, Tuscaloosa, AL 35487, USA*
[7]*Department of Physics, University of Zurich, 8057 Zurich, Switzerland*
[8]*Condensed Matter Theory Group, Paul Scherrer Institute, 5232 Villigen, Switzerland*
[9]*Institute for Theoretical Physics, ETH Zurich, 8093 Zurich, Switzerland*
[10]*Max Planck Institute for the Physics of Complex Systems, Nöthnitzer Str. 38, 01187 Dresden, Germany*

This supplemental material details the algorithm for constructing hyperbolic lattice flakes, the reason for interpreting type-II as BTZ geometry, our fit procedure, the derivation of Eqs. (2), (7), (8), (10), and (11), and the electrical circuit simulation.

CONTENTS

S1. DERIVATION OF EQ. (2)

We write the metric in isothermal coordinates as

$$ds^2 = g_{ij}dx^i dx^j = e^\varphi(dx^2 + dy^2) \tag{S1}$$

with $g_{ij} = e^\varphi \delta_{ij}$ and $i,j = 1,2$. We have $g^{ij} = e^{-\varphi}\delta_{ij}$ and $\sqrt{\det(g_{ij})} = e^\varphi$. Define the Gaussian curvature

$$\mathcal{K}[g] = -\frac{1}{2}e^{-\varphi}\nabla^2\varphi. \tag{S2}$$

The Poincaré disk metric

$$ds_\star^2 = (2\ell)^2 \frac{dx^2 + dy^2}{(1-|z|^2)^2}, \tag{S3}$$

$$\varphi_\star = \ln\left(\frac{(2\ell)^2}{(1-x^2-y^2)^2}\right) \tag{S4}$$

satisfies $\mathcal{K}[g_\star] = -\frac{1}{\ell^2}$.

The equations of motion associated to the Liouville action in Eq. (1) are

$$0 = \frac{\delta S_{\mathrm{LG}}}{\delta\varphi}[\varphi_\star] = -\nabla^2\varphi_\star + \frac{2}{\ell^2}e^{\varphi_\star}, \tag{S5}$$

which is equivalent to $\mathcal{K}[g_\star] = -\frac{1}{\ell^2}$, hence solved by the hyperbolic metric. We write $S_{\mathrm{LG}} = S_{\mathrm{kin}} + S_{\mathrm{pot}}$. Expanding $\varphi = \varphi_\star + \phi$ we obtain for the kinetic part

$$S_{\mathrm{kin}}[\varphi_\star + \phi] = \int d^2z \left[\frac{1}{2}[\nabla(\varphi_\star + \phi)]^2\right]$$

$$= \int d^2z \left[\frac{1}{2}(\nabla\varphi_\star)^2 + \nabla\varphi_\star \cdot \nabla\phi + \frac{1}{2}(\nabla\phi)^2\right]$$

$$= \int d^2z \left[-\frac{1}{2}\varphi_\star\nabla^2\varphi_\star - \phi\nabla^2\varphi_\star - \frac{1}{2}\phi\nabla^2\phi\right]$$

$$= \int d^2z\, e^{\varphi_\star}\left[-\frac{1}{2}\varphi_\star\frac{2}{\ell^2} - \phi\frac{2}{\ell^2} - \frac{1}{2}\phi(e^{-\varphi_\star}\nabla^2)\phi\right].$$

For the potential part we obtain

$$S_{\mathrm{pot}}[\varphi_\star + \phi] = \int d^2z \left[\frac{2}{\ell^2}e^{\varphi_\star}e^\phi\right] = \int d^2z\, e^{\varphi_\star}\left[\frac{2}{\ell^2}e^\phi\right].$$

Adding both expansions and neglecting terms that are independent of ϕ we obtain

$$S_{\mathrm{grav}}[\phi] = \int d^2z\, e^{\varphi_\star}\left[-\frac{1}{2}\phi(e^{-\varphi_\star}\nabla^2)\phi + \frac{2}{\ell^2}(e^\phi - \phi)\right]. \tag{S6}$$

Note that this action is again of Liouville form [1], but for a hyperbolic fiducial metric, whereas the starting action S_{LG} was based on a flat fiducial metric. This reflects the shift invariance of the Liouville action. However, due to the saddle-point expansion around $\varphi_\star$, fluctuations parametrized by ϕ are expected to be small, whereas this is not true for the field φ. Expanding the potential term in powers of ϕ we arrive at

$$S_{\text{grav}}[\phi] = \int \text{d}^2z \; e^{\varphi_\star} \Big[-\frac{1}{2}\phi(e^{-\varphi_\star}\nabla^2)\phi$$
$$+ \frac{2}{\ell^2}\Big(\frac{1}{2}\phi^2 + \frac{1}{3!}\phi^3 + \frac{1}{4!}\phi^4 + \dots\Big)\Big] \quad \text{(S7)}$$
$$= \int \frac{\text{d}^2z \; (2\ell)^2}{(1-|z|^2)^2} \Big[\frac{1}{2}\phi\Big(-\Box + \frac{2}{\ell^2}\Big)\phi$$
$$+ \frac{1}{3\ell^2}\phi^3 + \frac{1}{12\ell^2}\phi^4 + \dots\Big]. \quad \text{(S8)}$$

This is of the form of Eq. (2) after appropriate choice of constants m, u, μ, and normalization of ϕ. Here we used

$$e^{\varphi_\star} = \frac{(2\ell)^2}{(1-|z|^2)^2}, \quad \text{(S9)}$$

$$\Box = e^{-\varphi_\star}\nabla^2 = \frac{1}{(2\ell)^2}(1-|z|^2)^2\nabla^2. \quad \text{(S10)}$$

To connect the Liouville action to the lattice action

$$S(\{\phi_\mu\}) = -\frac{1}{2}\sum_{\mu,\nu}\phi_\mu A_{\mu\nu}\phi_\nu + \sum_\mu\Big(\frac{\hat{m}^2}{2}\phi_\mu^2 + \frac{u}{3!}\phi_\mu^3\Big), \quad \text{(S11)}$$

we replace $\sum_\nu A_{\mu\nu}\phi_\nu \to (q + qh^2\ell^2\Box)\phi_\mu$ [2] and find

$$S(\{\phi_\mu\}) = \sum_\mu\Big(\frac{1}{2}\phi_\mu(-qh^2\ell^2\Box - q + \hat{m}^2)\phi_\mu + \frac{u}{3!}\phi_\mu^3\Big)$$
$$= \sum_\mu\Big(qh^2\ell^2\frac{1}{2}\phi_\mu(-\Box + m^2)\phi_\mu + \frac{u}{3!}\phi_\mu^3\Big). \quad \text{(S12)}$$

We inserted $\hat{m}^2 = q + qh^2\ell^2m^2$. Through this equation, the experimental parameters $\hat{m}^2$ and u can be connected to the continuum Liouville action $S_{\text{grav}}[\phi]$.

S2. CONSTRUCTION OF TYPE-I AND II FLAKES

To construct hyperbolic flakes, we start from regular hyperbolic $\{p, q\}$ tilings with $(p-2)(q-2) > 4$, tessellated by p-sided polygons with q of them meeting at each site. We refer to type-I flakes as hyperbolic lattices with open boundary conditions, generated via vertex inflation [3–5] and embedded in the Poincaré disk

$$\mathbb{D} = \{z \in \mathbb{C}, \; |z| < 1\}, \quad \text{(S13)}$$

$$\text{d}s^2 = (2\ell)^2\frac{|\text{d}z|^2}{(1-|z|^2)^2}. \quad \text{(S14)}$$

Type-II flakes are constructed from the type-I flakes by identifying two geodesics related by a boost (as illustrated in Fig. 2a), akin to the construction of BTZ black holes from the AdS space. While such identification can be done by modifying the adjacency matrix of the lattice without a change of site coordinates, as the adjacency matrix alone encodes the lattice connectivity and thereby dictates the subsequent computation of correlation functions, we perform two conformal transformations of the site coordinates to facilitate the construction of finite-sized type-II flakes and clear visualization of their topologically nontrivial geometry.

In our analysis, we focus on the $\{3, 7\}$ tiling because using triangles as tiles allows every boundary site to be connected to a bulk site, leading to ample data for the correlation functions. We generate a finite-sized type-I $\{3, 7\}$ lattice, as depicted in Fig. 1a, via the vertex-inflation algorithm detailed in Ref. 5. Specifically, we implement six or seven iterations of vertex inflation (dubbed "shells"), resulting in a total of $N = 960$ or 2523 sites, respectively. We denote the adjacency matrix of the type-I lattice as A and the Poincaré disk coordinates as $\{z_\mu\}_{\mu=1}^N$.

We then proceed to construct type-II hyperbolic lattices from the 6-shell $\{3, 7\}$ type-I lattice. We first apply a conformal transformation $\mathcal{C}_1$ from the Poincaré disk to strip coordinates:

$$\mathcal{C}_1 : z \mapsto \zeta = \frac{2}{\pi}\ln\Big(\frac{1+z}{1-z}\Big), \quad \text{(S15)}$$

with domain and range

$$\mathcal{C}_1 : \mathbb{D} \to \mathbb{B} = \{\zeta \in \mathbb{C}, |\text{Im}(\zeta)| < 1\}. \quad \text{(S16)}$$

$\mathcal{C}_1$ maps 0 to 0 and the upper and lower halves of the Poincaré-disk boundary $z = e^{\text{i}\phi}$ to the lines $\text{i} + \mathbb{R}$ and $-\text{i} + \mathbb{R}$, respectively. The metric of the strip model is

$$\text{d}s^2 = \ell^2\Big(\frac{\pi}{2}\Big)^2\frac{|\text{d}\zeta|^2}{\cos^2\big(\frac{\pi}{2}\text{Im}(\zeta)\big)}, \quad \text{(S17)}$$

which diverges at the asymptotic boundary at $\text{Im}(\zeta) \to \pm 1$. The strip model is periodic along the x-direction with the period dependent on p and q. Given that our type-I lattice is finite-sized, the resultant strip model with site coordinates $\{\zeta_\mu\}_{\mu=1}^N$ (Fig. 1b) is non-uniform with progressively less complete asymptotic boundary away from $\text{Re}(\zeta) = 0$. Upon closer inspection, we identify two sites (highlighted in red in Fig. 1b) which lie on the left and right vertical edges that define a periodic segment. The difference of their coordinates gives the period $P \approx 1.845$ for the $\{3, 7\}$ tiling.

Our strategy is to create a mostly homogeneous type-II flake is to take the central periodic segment between the x-range $[-P/2, P/2)$, where the asymptotic boundaries at $\pm\text{i} + \mathbb{R}$ are the most complete, and copy this small segment k times, joining them together to form a long strip
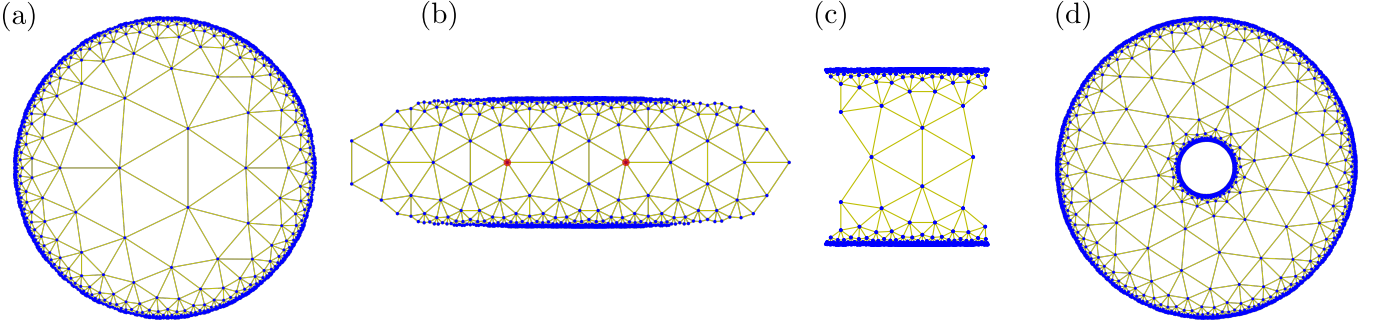
FIG. 1. **Construction of type-II hyperbolic lattices.** (a) A type-I hyperbolic lattice with $\{3, 7\}$ tessellation generated via finite iterations of vertex inflation. (b) After the conformal transformation in Eq. (S15), the finite-sized lattice is "squashed" into a finite strip with a discrete translation symmetry along the x-direction. The translation symmetry is incomplete due to the finite system size. The period P is given by the distance between the highlighted sites in red. (c) We isolate the central periodic segment in the range $x \in [-P/2, P/2)$ (shown here), where the CFT boundaries are the most complete, and join together k copies of the segment to form a finite periodic strip of width $w = kP$. (d) After joining the ends of the strip and passing the coordinates through a second conformal map defined in Eq. (S18), we arrive at a type-II hyperbolic lattice that represents the discretized time-slice of a BTZ black hole with temperature $T = kP/8\pi$.

of length kP. To achieve this, we single out those sites in Fig. 1b that lie outside the x-range $[-P/2, P/2)$ and truncate them from the adjacency matrix A by removing the corresponding rows and columns. We also remove these sites from the list of all coordinates $\{\zeta_\mu\}_{\mu=1}^N$. The truncated segment, shown in Fig. 1c, has $N' = 686$ sites; its adjacency matrix is denoted by a. Next, we begin building the adjacency matrix of the long strip, denoted $\tilde{A}$, by computing the Kronecker product of the $k \times k$ identity matrix and a: $\tilde{A} = \mathbb{1}_{k \times k} \otimes a$. The coordinates of the long strip are copies of the small-segment coordinates, shifted horizontally by integer multiples of P: 0, P, $2P$, ..., $(k-1)P$.

At this stage, our strip is formed from k disjoint segments. While the coordinates are correct, the adjacency matrix does not include edges connecting the neighboring segments to maintain a coordination number of 7 on every site. To connect the segments, we need to first determine the edges that were severed at the truncation step. The procedure is as follows. For each site μ in the truncated segment (Fig. 1c), we identify its nearest neighbors in the untruncated band (Fig. 1b) using the original adjacency matrix A. If a particular nearest neighbor ν is not included in the truncated segment, we numerically search for the site ν' such that it belongs to the segment and equivalent to ν modulo horizontal translation defined by the periodicity. Note that during this identification process, we set the numerical tolerance in distance comparison to 10^{-10}. We record all the severed edges on the right side of the truncated segment in a list (μ, ν'). We also check that the severed edges on the left side correspond to the same set of edges. Finally, we re-introduce these severed edges to the adjacency matrix $\tilde{A}$ between every pair of neighboring segments centered at cP and $(c+1)P$ for $c = 0, ..., k-2$, as well as the pair at the ends centered at $(k-1)P$ and 0 to respect the

periodic boundary condition. At this stage, $\tilde{A}$ correctly describes a type-II lattice with kN' sites.

We apply another conformal transformation $\mathcal{C}_2$ to wrap the strip model into an annulus geometry (Fig. 1d):

$$\mathcal{C}_2 : \zeta \mapsto \hat{z} = e^{2\pi i(\zeta + i)/(kP)}, \tag{S18}$$

with domain and range

$$\mathcal{C}_2 : \mathbb{B} \to \mathbb{A} = \{\hat{z} \in \mathbb{C}, \ \hat{r}_0 < |\hat{z}| < 1\}. \tag{S19}$$

$\mathcal{C}_2$ maps the upper boundary $i + \mathbb{R}$ in the strip model to the inner boundary of the annulus at radius $\hat{r}_0 = \mathcal{C}_2(i) = e^{-4\pi/(kP)}$ and the lower boundary $-i + \mathbb{R}$ to the outer boundary at 1. The new metric is

$$ds^2 = \left(\frac{\ell kP}{4}\right)^2 \frac{|d\hat{z}|^2}{|\hat{z}|^2 \cos^2\left(\frac{\pi}{2}(1 + \frac{kP}{2\pi}\log|\hat{z}|)\right)} \tag{S20}$$

$$= \left(\frac{\ell kP}{4}\right)^2 \frac{|d\hat{z}|^2}{|\hat{z}|^2 \sin^2\left(\frac{kP}{4}\log|\hat{z}|\right)},$$

which diverges at the boundaries $|\hat{z}| = \hat{r}_0$ and 1. The circle separating the inner and outer halves of the type-II lattice is at radius

$$\hat{r}_H = \mathcal{C}_2(0) = e^{-2\pi/(kP)} = \sqrt{\hat{r}_0}, \tag{S21}$$

which can be interpreted as the black hole horizon.

S3. RELATION BETWEEN TYPE-II AND BTZ GEOMETRY

In this section, we show that timeslices of the three-dimensional BTZ black hole correspond to the type-II geometry simulated on our hyperbolic lattices. For this purpose, we first recall some facts about the BTZ solution

following Ref. [6], and then show explicitly how timeslices are embedded in the Poincaré upper half-plane and disk models, $\mathbb{H}$ and $\mathbb{D}$, respectively.

We consider the imaginary-time BTZ black hole, which is a solution to the imaginary-time Einstein equations in vacuum in $2 + 1$ spacetime dimensions for a negative cosmological constant $\Lambda = -1/\ell^2$, given by the metric

$$ds_{\mathrm{BTZ}}^2 = \left(\frac{\rho^2}{\ell^2} - M\right)d\tau^2 + \left(\frac{\rho^2}{\ell^2} - M\right)^{-1}d\rho^2 + \rho^2 d\vartheta^2.$$
(S22)

Here M is a dimensionless parameter and $\rho \geq \rho_{\mathrm{H}}$ is a non-compact radial coordinate that describes the region outside the event horizon, which is located at the singular radius

$$\rho_{\mathrm{H}} = \sqrt{M}\ell.$$
(S23)

The imaginary time and radial coordinates, τ and ϑ, are compactified to the intervals $\tau \in [0, 2\pi\ell^2/\rho_{\mathrm{H}})$ and $\vartheta \in [0, 2\pi)$ through the identifications

$$(\rho, \tau, \vartheta) \sim \left(\rho, \tau + 2\pi\frac{\ell^2}{\rho_{\mathrm{H}}}, \vartheta\right),$$
(S24)

$$(\rho, \tau, \vartheta) \sim (\rho, \tau, \vartheta + 2\pi).$$
(S25)

The periodicity in τ with period T^{-1} corresponds to a black hole temperature

$$T = \frac{\rho_{\mathrm{H}}}{2\pi\ell^2} = \frac{\sqrt{M}}{2\pi\ell}.$$
(S26)

As any solution to the vacuum Einstein field equations in 2+1 dimensions with negative cosmological constant, the BTZ black hole is equivalent to a quotient $\mathcal{H}_3/\sim$, where $\mathcal{H}_3$ is hyperbolic three-space with constant negative curvature, and $\sim$ is an equivalence relation. Here we denote $\mathcal{H}_3$ in the upper half-space coordinates

$$\mathcal{H}_3 = \{(x, y, z) \in \mathbb{R}^3, \ z > 0\},$$
(S27)

$$ds^2 = \frac{\ell^2}{z^2}(dx^2 + dy^2 + dz^2).$$
(S28)

The equivalence is made explicit by the coordinate transformation

$$x = \left(1 - \frac{\rho_{\mathrm{H}}^2}{\rho^2}\right)^{1/2}\cos\left(\frac{\rho_{\mathrm{H}}\tau}{\ell^2}\right)e^{\sqrt{M}\vartheta},$$

$$y = \left(1 - \frac{\rho_{\mathrm{H}}^2}{\rho^2}\right)^{1/2}\sin\left(\frac{\rho_{\mathrm{H}}\tau}{\ell^2}\right)e^{\sqrt{M}\vartheta},$$
(S29)

$$z = \frac{\rho_{\mathrm{H}}}{\rho}e^{\sqrt{M}\vartheta}.$$

The identification in Eqs. (S24) and (S25) limits the image to a region $\mathcal{S}_3/\sim$ given by

$$\mathcal{S}_3 = \left\{(x, y, z) \in \mathcal{H}_3, \ 1 \leq \sqrt{x^2 + y^2 + z^2} < e^{2\pi\sqrt{M}}\right\}$$
(S30)

with the identification

$$(x, y, z) \sim e^{2\pi\sqrt{M}}(x, y, z).$$
(S31)

This consists of the region between two hemispheres in the upper half-space, where the inner and outer hemisphere are identified such that identified points lie on rays in $\mathcal{H}_3$ that go through the origin $(0, 0, 0)$. Timeslices of the BTZ geometry with a fixed value of τ correspond to $d\tau = 0$ in Eq. (S22), They are described by the static black hole metric

$$ds^2 = \left(\frac{\rho^2}{\ell^2} - M\right)^{-1}d\rho^2 + \rho^2 d\vartheta^2.$$
(S32)

Embedding timeslices into $\mathbb{H}$. We define the two-dimensional Poincaré upper half-plane model through

$$\mathbb{H} = \{x + iz \in \mathbb{C}, \ z > 0\},$$
(S33)

$$ds^2 = \frac{\ell^2}{z^2}(dx^2 + dz^2).$$
(S34)

Choosing $\tau_+ = 0$ or $\tau_- = \frac{1}{2}T^{-1} = \frac{\pi\ell^2}{\rho_{\mathrm{H}}}$ in Eqs. (S29) yields

$$x = \pm\left(1 - \frac{\rho_{\mathrm{H}}^2}{\rho^2}\right)^{1/2}e^{\sqrt{M}\vartheta},$$

$$y = 0,$$
(S35)

$$z = \frac{\rho_{\mathrm{H}}}{\rho}e^{\sqrt{M}\vartheta},$$

where the plus (minus) sign in x corresponds to τ_+ (τ_-). Discarding the y-variable, this yields Universes I and II embedded into $\mathbb{H}$ given by $\mathcal{S}_{2,\mathrm{I}}/\sim$ and $\mathcal{S}_{2,\mathrm{II}}/\sim$, respectively, with

$$\mathcal{S}_{2,\mathrm{I}} = \{(x, z) \in \mathbb{H}, \ 1 \leq \sqrt{x^2 + z^2} < e^{2\pi\sqrt{M}}, \ x > 0\},$$
(S36)

$$\mathcal{S}_{2,\mathrm{II}} = \{(x, z) \in \mathbb{H}, \ 1 \leq \sqrt{x^2 + z^2} < e^{2\pi\sqrt{M}}, \ x < 0\}$$
(S37)

and the identification

$$(x, z) \sim e^{2\pi\sqrt{M}}(x, z).$$
(S38)

The event horizon ($\rho = \rho_{\mathrm{H}}$) corresponds to the topological circle $\mathcal{S}_{2,\mathrm{H}}/\sim$ with

$$\mathcal{S}_{2,\mathrm{H}} = \{(0, z) \in \mathbb{H}, \ 1 \leq z < e^{2\pi\sqrt{M}}\}.$$
(S39)

This corresponds to a region between two geodesics (circular arcs) that are identified. See Fig. 2a for a visualization.

Embedding timeslices into $\mathbb{D}$. We achieved to show that timeslices $\tau_\pm$ corresponds to the region between two geodesics that are identified. This is the starting point of the squash-and-wrap procedure and thus proves the
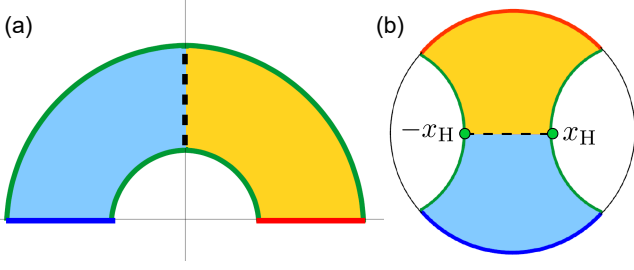
FIG. 2. Timeslice of the BTZ black hole with $\tau = 0$ after mapping to the upper half-plane model $\mathbb{H}$ (left) and Poincaré disk model $\mathbb{D}$ (right). Points along the geodesics indicated in green are identified; this reveals the quotient structure of the geometry. We show the points $\pm x_\mathrm{H}$ in $\mathbb{D}$ that are mapped to $\pm w/2$ in the strip coordinates under $\mathcal{C}_2$, which gives the relation $T = w/(8\pi\ell)$.

equivalence to the type-II geometry. To make the correspondence even clearer, we formulate the timeslices in the Poincaré disk geometry. The mapping between $\mathbb{H}$ and $\mathbb{D}$ is facilitated by the Cayley transformation.

$$\mathbb{H} \;\to\; \mathbb{D}, \tag{S40}$$

$$w \;\mapsto\; z = \frac{w - \mathrm{i}}{w + \mathrm{i}}. \tag{S41}$$

Here we work with the complex conjugate of the Cayley map for convenience and choose $\vartheta \in [-\pi, \pi)$ to obtain a more symmetric image. The mapping in Eqs. (S35) translate to Poincaré disk coordinates $z = x + \mathrm{i}y \in \mathbb{D}$ with

$$x = \frac{\frac{\rho}{\rho_\mathrm{H}} \sinh(\sqrt{M}\vartheta)}{1 + \frac{\rho}{\rho_\mathrm{H}} \cosh(\sqrt{M}\vartheta)}, \tag{S42}$$

$$y = \frac{\pm 1 \sqrt{\frac{\rho^2}{\rho_\mathrm{H}^2} - 1}}{1 + \frac{\rho}{\rho_\mathrm{H}} \cosh(\sqrt{M}\vartheta)}. \tag{S43}$$

The static BTZ metric in Eq. (S32) is mapped to the hyperbolic metric

$$\mathrm{d}s^2 = (2\ell)^2 \frac{|\mathrm{d}z|^2}{(1 - |z|^2)^2}. \tag{S44}$$

The image splits into Universes I and II in $\mathbb{D}$ with points along a geodesic identified, see Figs. 1b and 2b. Along the horizon with $\rho = \rho_\mathrm{H}$ we have $y = 0$ and $-x_\mathrm{H} \leq x < x_\mathrm{H}$ with opposite ends identified, and

$$x_\mathrm{H} = \tanh\left(\frac{\rho_\mathrm{H}\vartheta_{\max}}{2\ell}\right) = \tanh\left(\frac{\rho_\mathrm{H}\pi}{2\ell}\right). \tag{S45}$$

Under the map $\mathcal{C}_2$ from Eq. (S18), x_H is mapped to the point $\frac{w}{2}$ in the strip geometry, and hence

$$\frac{w}{2} = \mathcal{C}_2(x_\mathrm{H}) = \frac{2}{\pi} \ln\left(\frac{1 + x_\mathrm{H}}{1 - x_\mathrm{H}}\right) = \frac{4}{\pi} \frac{\rho_\mathrm{H}\pi}{2\ell} = \frac{2\rho_\mathrm{H}}{\ell}. \tag{S46}$$

Using Eq. (S26), we conclude that the relation between T and w in the type-II geometries is given by

$$T = \frac{w}{8\pi\ell}. \tag{S47}$$

S4. DERIVATION OF EQS. (7) AND (8)

We divide the graph $\mathcal{G}$ into bulk (interior) and boundary and use the following notation:

graph	site index
$\mathcal{G} = \mathring{\mathcal{G}} \cup \partial\mathcal{G}$	$\mu, \nu, \ldots$
$\mathring{\mathcal{G}}$	$i, j, \ldots$
$\partial\mathcal{G}$	$, b, \ldots$

The quadratic part of the action is

$$S_0(\{\phi_\mu\}) = \frac{1}{2} \sum_{\mu,\nu} M_{\mu\nu} \phi_\mu \phi_\nu \tag{S48}$$

with $M = -A + \omega\mathbb{1}$ a real symmetric matrix. We set the values of ϕ_a on $\partial\mathcal{G}$ to J_a and consider the generating function

$$Z_0(\{J_a\}) = \int \left(\prod_i \mathrm{d}\phi_i\right) e^{-S_0(\{\phi_i, \phi_a = J_a\})}$$

$$= e^{-S_{0,\mathrm{eff}}(\{J_a\})} \tag{S49}$$

with

$$S_{0,\mathrm{eff}} = \frac{1}{2} \sum_{a,b} \left(M_{ab} - \sum_{i,j} M_{ai} G_{ij} M_{jb}\right) J_a J_b \tag{S50}$$

and $G_{ij} = (M^{-1})_{ij}$.

Boundary two-point function. We obtain the non-interacting two-point boundary correlator

$$\langle \mathcal{O}_a \mathcal{O}_b \rangle_0 = \frac{\partial^2 \ln Z_0}{\partial J_a \partial J_b} = -\frac{\partial^2 S_{\mathrm{eff}}}{\partial J_a \partial J_b}$$

$$= -M_{ab} + \sum_{i,j} M_{ai}(M^{-1})_{ij} M_{jb}. \tag{S51}$$

For $u = 0$ this coincides with $\langle \mathcal{O}_a \mathcal{O}_b \rangle$ and yields Eq. (7). We neglect here the subleading self-energy term that arises for $u \neq 0$, as is commonly done in holographic studies.

Boundary three-point function. Note that the non-interacting three-point boundary correlator vanishes,

$$\langle \mathcal{O}_a \mathcal{O}_b \mathcal{O}_c \rangle_0 = \frac{\partial^3 \ln Z_0}{\partial J_a \partial J_b \partial J_c} = 0, \tag{S52}$$

as do higher n-point functions. Including the cubic interaction term we have

$$S(\{\phi_\mu\}) = S_0(\{\phi_\mu\}) + \frac{u}{3!} \sum_\mu \phi_\mu^3. \tag{S53}$$

We treat interactions perturbatively according to

$$Z(\{J_a\})$$

$$= e^{-\frac{u}{3!}\sum_a J_a^3}\int\Big(\prod_i \mathrm{d}\phi_i\Big)e^{-S_0(\{\phi_i,J_a\})-\frac{u}{3!}\sum_i \phi_i^3}$$

$$\simeq e^{-\frac{u}{3!}\sum_a J_a^3}\int\Big(\prod_i \mathrm{d}\phi_i\Big)\Big(1-\frac{u}{3!}\sum_j \phi_j^3\Big)e^{-S_0(\{\phi_i,J_a\})}$$

$$= e^{-\frac{u}{3!}\sum_a J_a^3}Z_0(\{J_a\})\Big(1-\frac{u}{3!}\sum_i \langle\phi_i^3\rangle_0\Big). \qquad (S54)$$

We have

$$\langle\phi_i^3\rangle_0 = 3\langle\phi_i^2\rangle_{0,\mathrm{con}}\langle\phi_i\rangle_0 + \langle\phi_i\rangle_0\langle\phi_i\rangle_0\langle\phi_i\rangle_0 \qquad (S55)$$

$$=: \sum_a J_a w_a^{(i)} + \sum_{a,b,c} J_a J_b J_c w_{abc}^{(i)} \qquad (S56)$$

with "con" indicating the connected correlation function. We show below that

$$\langle\phi_i\rangle_0 = -\sum_a\sum_j J_a M_{aj}(M^{-1})_{ji}, \qquad (S57)$$

$$\langle\phi_i\phi_j\rangle_0 = (M^{-1})_{ij} + \langle\phi_i\rangle_0\langle\phi_j\rangle_0, \qquad (S58)$$

$$\langle\phi_i\phi_j\rangle_{0,\mathrm{con}} = (M^{-1})_{ij}, \qquad (S59)$$

whereas $\langle\phi_i^3\rangle_{0,\mathrm{con}} = 0$. We then obtain

$$w_a^{(i)} = -3M_{ii}\sum_j M_{aj}G_{ji}, \qquad (S60)$$

$$w_{abc}^{(i)} = -\Big(\sum_j M_{aj}G_{ji}\Big)\Big(\sum_k M_{bk}G_{ki}\Big)\Big(\sum_l M_{cl}G_{li}\Big), \qquad (S61)$$

the latter being symmetric in the indices a, b, c. The perturbative generating function becomes

$$Z \simeq e^{-\frac{u}{3!}\sum_a J_a^3}Z_0\Big(1-\frac{u}{3!}\sum_i\sum_a J_a w_a^{(i)}$$

$$-\frac{u}{3!}\sum_i\sum_{a,b,c} J_a J_b J_c w_{abc}^{(i)}\Big). \qquad (S62)$$

We re-exponentiate this to obtain

$$\ln Z \simeq -\frac{1}{3!}\sum_a u J_a^3 - S_{0,\mathrm{eff}} - \frac{u}{3!}\sum_i\sum_a J_a w_a^{(i)}$$

$$-\frac{u}{3!}\sum_i\sum_{a,b,c} J_a J_b J_c w_{abc}^{(i)}. \qquad (S63)$$

We then find

$$\langle\mathcal{O}_a\mathcal{O}_b\mathcal{O}_c\rangle = \frac{\partial^3 \ln Z}{\partial J_a \partial J_b \partial J_c} = -u\delta_{ab}\delta_{ac} - u\sum_i w_{abc}^{(i)}. \qquad (S64)$$

For $a \neq b$ we arrive at

$$\langle\mathcal{O}_a\mathcal{O}_b\mathcal{O}_c\rangle$$

$$= u\sum_i\Big(\sum_j M_{aj}G_{ji}\Big)\Big(\sum_k M_{bk}G_{ki}\Big)\Big(\sum_l M_{cl}G_{li}\Big), \qquad (S65)$$

which is Eq. (8).

Correlation functions of ϕ with sources. We now derive Eqs. (S57)-(S59). To compute correlation functions of bulk fields ϕ_i in the presence of boundary sources J_a, we introduce auxiliary bulk sources h_i according to

$$Z_0(\{J_a, h_i\}) = \int\Big(\prod_i \mathrm{d}\phi_i\Big)e^{-S_0(\{\phi_i,J_a\})+\sum_i h_i\phi_i} \qquad (S66)$$

$$= e^{-S_{0,\mathrm{eff}}[J]-\sum_{i,j}\sum_a M_{ai}J_a(M^{-1})_{ij}h_j+\frac{1}{2}\sum_{i,j}(M^{-1})_{ij}h_i h_j} \qquad (S67)$$

and correlation functions are obtained from

$$\langle\phi_{i_1}\cdots\phi_{i_n}\rangle_0 = \frac{\partial^n Z_0}{\partial h_{i_1}\cdots\partial h_{i_n}}\Big|_{h=0}, \qquad (S68)$$

$$\langle\phi_{i_1}\cdots\phi_{i_n}\rangle_{0,\mathrm{con}} = \frac{\partial^n \ln Z_0}{\partial h_{i_1}\cdots\partial h_{i_n}}\Big|_{h=0}. \qquad (S69)$$

This yields Eqs. (S57)-(S58). All connected n-point functions of ϕ_i vanish, because $\ln Z_0$ is quadratic in h.

S6. DERIVATION OF EQ. (10)

In this section we discuss the expected behavior of the 2-pt function $\langle\mathcal{O}_a\mathcal{O}_b\rangle$ for both type-I and type-II geometries in the continuum. This enables the identification of the respective expressions for d_{ab} in Eq. (10). Our approach is based on the observation that the two-point function asymptotically behaves like $\langle\mathcal{O}_a\mathcal{O}_b\rangle \simeq e^{-\Delta\sigma_{ab}/\ell}$, where σ_{ab} is the large geodesic distance between two sites z_a and z_b. The latter, however, can be computed in the continuum for any two sites z and z'.

Both type-I and type-II geometries are locally AdS, with a Riemannian (all-positive) signature. The equation of motion of real scalar fields in the bulk are expressed through the Laplace–Beltrami operator $\Box = (1/\sqrt{\det(g)})\partial_\mu(\sqrt{\det(g)}g^{\mu\nu}\partial_\nu)$. The bulk Green function satisfies

$$\left(-\Box + m^2\right)G(Z;Z') = \frac{1}{\sqrt{\det(g)}}\delta^{(d+1)}(Z-Z'). \qquad (S70)$$

where Z denotes the generalized coordinate of the AdS$_2$ with $d = 1$. For general AdS$_{d+1}$, the solution is

$$G(Z;Z') = G(\xi(Z,Z')), \qquad (S71)$$

$$G(\xi) = \xi^\Delta \,_2F_1\Big(\Delta, \frac{d}{2}; \Delta+1-\frac{d}{2}; \xi\Big),$$

where $m^2\ell^2 = \Delta(\Delta-d)$, and $0 \leq \xi(Z,Z')^{-1} = \cosh(\sigma(Z,Z')/\ell) \leq 1$ is a dimensionless parameter, determined by the geodesic distance $\sigma(Z,Z')$ [7]. The hypergeometric function is denoted by $_2F_1$. For large σ, the term containing $_2F_1$ can be neglected and we have $G(\sigma) \simeq \xi^\Delta \simeq e^{-\Delta\sigma/\ell}$.

<u>Type-I geometry.</u>—The geodesic distance in the Poincaré disk with metric

$$\mathrm{d}s_\mathrm{I}^2 = \frac{(2\ell)^2}{(1-|z|^2)^2}|\mathrm{d}z|^2 \qquad (\mathrm{S72})$$

is given by

$$\sigma(z,z') = \ell \,\mathrm{arcosh}\Big(1 + \frac{2|z-z'|^2}{(1-r^2)(1-r'^2)}\Big). \qquad (\mathrm{S73})$$

For sites close to the boundary, $r, r' \to 1$, we can use $\mathrm{arcosh}(x) \simeq \ln(2x)$ for $x \gtrsim 4$, to approximate this as

$$\sigma(z,z') \simeq \ell \,\ln\Big(\frac{4|z-z'|^2}{(1-r^2)(1-r'^2)}\Big). \qquad (\mathrm{S74})$$

The corresponding correlation function reads

$$G(z;z') \simeq \Big(\frac{(1-r^2)(1-r'^2)}{4|z-z'|^2}\Big)^\Delta. \qquad (\mathrm{S75})$$

For two sites $z = re^{\mathrm{i}\theta}$ and $z' = r'e^{\mathrm{i}\theta'}$ close to the boundary, we then obtain the boundary 2-pt function

$$G(\theta,\theta') \simeq \frac{\tilde{C}_2}{|e^{\mathrm{i}\theta} - e^{\mathrm{i}\theta'}|^{2\Delta}}. \qquad (\mathrm{S76})$$

Comparing this with

$$G(\theta_a,\theta_b) \simeq \frac{\bar{C}_2}{(d_{ab})^{2\Delta}} \qquad (\mathrm{S77})$$

leads to the first line of Eq. (10).

The coefficient $\tilde{C}_2$ depends on r, r' and, technically, vanishes as $r, r' \to 1$. In the continuum, choosing the boundary on a circle of radius $R < 1$, this can be absorbed by a redefinition of the field, while on the discrete lattice (due to the variation in the discrete r_i), there is a

residual dependence of $\langle \mathcal{O}_a \mathcal{O}_b \rangle$ on r_a and r_b. This effect, however, is small for large enough flakes.

<u>Type-II geometry.</u> The continuum geometry of the type-II lattice (Eq. 4 and Eq. S20) can be parametrized in angular coordinates $\hat{z} = \hat{r}e^{i\theta}$ through the metric

$$\begin{aligned}\mathrm{d}s_\mathrm{II}^2 &= \Big(\frac{\ell w}{4}\Big)^2 \frac{\mathrm{d}\hat{r}^2 + \hat{r}^2\mathrm{d}\theta^2}{\hat{r}^2 \sin^2\big(\frac{w}{4}\log\hat{r}\big)} \\ &= \ell^2 \frac{\mathrm{d}[\frac{w}{4}\log\hat{r}]^2 + \mathrm{d}[\frac{w}{4}\theta]^2}{\sin^2\big(\frac{w}{4}\log\hat{r}\big)},\end{aligned} \qquad (\mathrm{S78})$$

with $w = kP = 8\pi T\ell$ as defined in Eq. (S47). The locally-AdS geometry can also be described by the upper half-plane metric

$$\mathrm{d}s_\mathrm{II}^2 = \frac{\ell^2}{y^2}\left(\mathrm{d}x^2 + \mathrm{d}y^2\right), \qquad (\mathrm{S79})$$

from which the angle-coordinate metric [Eq. (S78)] of the same geometry is obtained by the coordinate transformations,

$$\begin{aligned} x &= e^{w\theta/4}\cos\Big(\frac{w}{4}\log\hat{r}\Big), \\ y &= e^{w\theta/4}\sin\Big(\frac{w}{4}\log\hat{r}\Big). \end{aligned} \qquad (\mathrm{S80})$$

The coordinate transformation also provides a map to the type-II Green function from the corresponding function expressed in terms of the upper half-plane geodesic distances. For two sites on the Poincaré upper half-plane, (x,y) and (x',y'), the Green function for long distances is given by [7]

$$G(x,y;x',y') \simeq \Big(\frac{2yy'}{y^2 + y'^2 + (x-x')^2}\Big)^\Delta. \qquad (\mathrm{S81})$$

Define $\chi = \frac{w}{4}\log\hat{r}$, hence $(x,y) = e^{w\theta/4}(\cos\chi, \sin\chi)$, so that the Green function becomes

$$G(\chi,\theta;\chi',\theta') \simeq \left(\frac{2\sin\chi\sin\chi' e^{\frac{w}{4}(\theta+\theta')}}{e^{\frac{w}{2}\theta}\sin^2\chi + e^{\frac{w'}{2}\theta'}\sin^2\chi' + (e^{\frac{w}{4}\theta}\cos\chi - e^{\frac{w}{4}\theta'}\cos\chi')^2}\right)^\Delta. \qquad (\mathrm{S82})$$

To approach the outer boundary of the type-II graph, $\hat{r} \to 1$, we introduce an infrared regulator ε according to $\hat{r} = e^{-4\pi\varepsilon/w}$ or, equivalently, $\chi = -\pi\varepsilon$. The two-point function on the boundary becomes

$$G(\theta,\theta') \simeq \lim_{\varepsilon,\varepsilon'\to 0}\left(\frac{2\pi^2\varepsilon\varepsilon'}{[\sinh\pi T\ell(\theta-\theta')]^2}\right)^\Delta. \qquad (\mathrm{S83})$$

As in the type-I case, the vanishing prefactor as $\varepsilon, \varepsilon' \to 0$ can be absorbed into a redefinition of the boundary field. By enforcing angular periodicity via the method of

images, we obtain the 2-point function between between boundary sites θ_a and θ_b as

$$G(\theta_a,\theta_b) \simeq \bar{C}_2 \sum_{n\in\mathbb{Z}}\Big(\frac{1}{\sinh[\pi T\ell(\theta_a - \theta_b + 2\pi n)]}\Big)^{2\Delta}. \qquad (\mathrm{S84})$$

This form validates the choice of d_{ab} for the type-II graphs in Eq. (10).

S5. DERIVATION OF EQ. (11)

To derive Eq. (11), we extend the presentations in Refs. [2, 8]. We consider the non-interacting part of the lattice action $S(\{\phi_\mu\})$ and consider the equation of motion for the field on a bulk site $z_i \in \mathbb{D}$ with q neighbors given by

$$-\sum_\mu A_{\mu i}\phi(z_i) + \hat{m}^2\phi(z_i) = 0. \tag{S85}$$

This can be written as

$$\sum_{\alpha=1}^{q} \phi\left(\frac{z_i - w_\alpha}{1 - w_\alpha \bar{z}_i}\right) = \hat{m}^2\phi(z_i), \tag{S86}$$

where the sum extends over the neighbors of z_i. Here $w_\alpha = he^{2\pi(\alpha-1)\mathrm{i}/q}e^{\mathrm{i}\chi_i}$ and χ_i a defect angle that depends on z_i. The dimensionless parameter h is a lattice constant given by

$$h = \left(1 - \frac{\sin^2(\frac{\pi}{q})}{\cos^2(\frac{\pi}{p})}\right)^{1/2}. \tag{S87}$$

The expression on the left-hand side of Eq. (S86) can be expanded in powers of h with the universal leading term given by [2]

$$\left(q + qh^2\ell^2\Box + O(h^3)\right)\phi(z_i) = \hat{m}^2\phi(z_i). \tag{S88}$$

This is equivalent to the Klein–Gordon type equation

$$(-\Box + m^2)\phi(z) = 0 \tag{S89}$$

through the identification

$$\hat{m}^2 = q + qh^2m^2\ell^2. \tag{S90}$$

We define the dimensionless Laplacian $\hat{\Box} = \ell^2\Box$. In the Poincaré disk with $z = x + \mathrm{i}y \in \mathbb{D}$ we have $\hat{\Box} = \frac{1}{4}(1 - |z|^2)^2(\partial_x^2 + \partial_y^2) = (1 - |z|^2)^2\partial_z\bar{\partial}_z$. Eigenfunctions of $\hat{\Box}$ are labelled by a real quantum number Δ such that $\hat{\Box}\phi_\Delta(z) = \Delta(\Delta - 1)\phi_\Delta(z)$. (This is most easily seen in upper half-plane coordinates $x + \mathrm{i}y \in \mathbb{H}$ with $\hat{\Box} = y^2(\partial_x^2 + \partial_y^2)$ and $\phi_\Delta(x, y) = y^\Delta$.) We have

$$\left(q + qh^2\frac{\Delta(\Delta - 1)}{\ell^2} + O(h^3)\right)\phi_\Delta(z_i) = \hat{m}^2\phi_\Delta(z_i), \tag{S91}$$

or,

$$\Delta(\Delta - 1) + O(h) = m^2\ell^2, \tag{S92}$$

which recovers the universal continuum limit result.

Higher orders in an expansion in the parameter h in Eq. (S88) can be derived. Importantly, terms that are not powers of $\hat{\Box}$ appear at order h^q, and so the power series

needs to be stopped earlier. For the $\{3, 7\}$ tessellation with $q = 7$ we have

$$q\left(1 + h^2\hat{\Box} + \frac{h^4}{4}(\hat{\Box}^2 + 2\hat{\Box})\right. \tag{S93}$$

$$\left. + \frac{h^6}{36}(\hat{\Box}^3 + 10\hat{\Box}^2 + 12\hat{\Box}) + O(h^7)\right)\phi(z_i) = \hat{m}^2\phi(z_i), \tag{S94}$$

which is of the form

$$q + qh^2 f(\hat{\Box})\phi(z_i) = \hat{m}^2\phi(z_i) \tag{S95}$$

with $f(X)$ given in Eq. (10). Acting on eigenfunctions ϕ_Δ we obtain

$$f(\Delta(\Delta - 1))\phi_\Delta = m^2\ell^2\phi_\Delta, \tag{S96}$$

and hence the lattice relation between Δ and $m^2\ell^2$. For a general $\{p, q\}$ lattice, the expansion reads

$$f(X) = \sum_{l=1}^{l_{\max}} \frac{h^{2(l-1)}}{l!^2}T_l(X) + O(h^{q-2}), \tag{S97}$$

which has to be stopped at order $l_{\max}$ such that $2(l_{\max} - 1) < q - 1$. For instance $q = 3$ means $l_{\max} = 1$ and $q = 7$ means $l_{\max} = 3$. The polynomials $T_l(X)$ are

$$T_1(X) = X, \tag{S98}$$
$$T_2(X) = X^2 + 2X, \tag{S99}$$
$$T_3(X) = X^3 + 10X^2 + 12X, \tag{S100}$$
$$T_4(X) = X^4 + 28X^3 + 156X^2 + 144X. \tag{S101}$$

They can be computed systematically to arbitrary order from a Taylor expansion of Eq. (S86).

S7. FIT PROCEDURE

Type-I / Zero temperature

2-point functions.—We first check the scaling form of the 2-pt functions on the boundary by tuning the bulk scalar mass. In Fig. 3, we verify the scaling behavior

$$\langle\mathcal{O}_a\mathcal{O}_b\rangle \simeq \frac{\bar{C}_2}{|e^{\mathrm{i}\theta_a} - e^{\mathrm{i}\theta_b}|^{2\Delta}} \tag{S102}$$

for $\langle\mathcal{O}_a\mathcal{O}_b\rangle$ obtained from Eq. (7) in the main text, with the two boundary points θ_a and θ_b on the Poincaré disk. Fig. 3 uses a binning of the correlation function dataset to reduce small-distance discretization effects. We consider different sample sizes for the binning and perform a least-square fitting of the data on a logarithmic grid. We pick the binning with the least net residual for each dataset depicted in Fig. 3 (a). While the binning reduces the
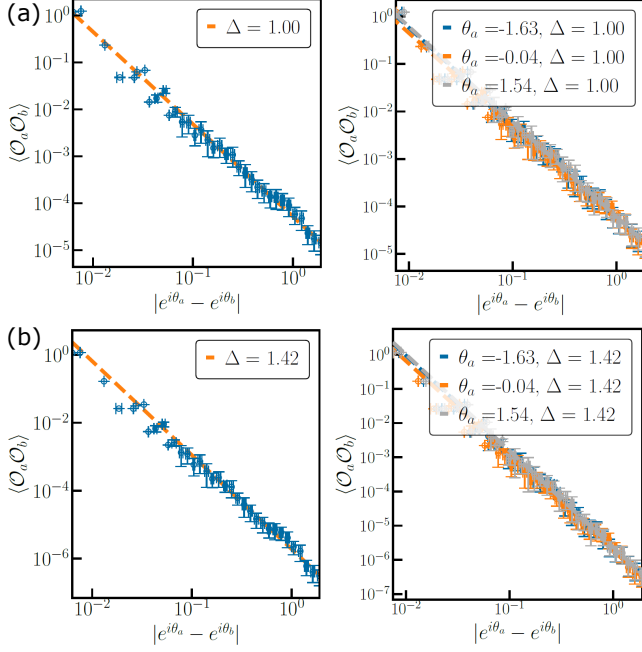
FIG. 3. The power-law scaling of the 2-point boundary correlation functions obtained from Eq. (7), between two boundary points a and b. In **(a)** and **(b)**, the function on a type-I flake with 6 shells are shown with bulk scalar masses $m^2\ell^2 = 0.01$ and 0.74, respectively. The quoted values of Δ are the fitted values. On the left panels, a fixed boundary site at $\theta_a = 0$ is chosen as a reference. On the right panels, three separate angular positions have been chosen for a, as the site b crawls along the boundary. The discreteness of the boundary introduces small amplitude variations but the scaling dimension remains largely unaffected, demonstrating the expected CFT behavior at zero temperature. The scatter (depicted as error bars) results from the binning of the boundary distances. Note that $m = 0$ is consistent with $\Delta = 1$.

FIG. 4. The conformal scaling of the 3-point function computed from Eq. (8), applied to type-I graphs with 7 shells for masses $m^2\ell^2 = 0.01$, 0.48, and 0.90, plotted respectively in **(a)**, **(b)**, and **(c)**. The figures depict the correlation function for two fixed boundary sites a and c, with a third site b that moves along the boundary. In **(a)**, the function is plotted against the relative distance between the a and b coordinates, depicting the contact divergence when b coincides with the third coordinate c. In **(b)** and **(c)**, a scaling collapse over the product of the pairwise relative distances, fitted as the dashed grey lines, shows a remarkable agreement with the solid orange lines defined by the scaling dimension obtained from the 2-point function.

scatter in the local magnitudes of the correlation function, the discrete lattice also introduces a ruggedness in the boundary geometry that requires further consideration. However, this effect is mitigated by sampling over several distinct pairs of boundary locations that share the same global distances. In effect, we fix the location of one site a, and let the other site b move all the way across the compact boundary. The right-hand panels in Fig. 3 depict the variation of the 2-point function for three such choices of the anchored site a. By averaging through many such boundary reference frames distinguished by the anchoring of their origin coordinates a, we obtain the mass parametrization of the scaling dimension Δ that is depicted in the main text along with its related standard deviation.

3-point functions.—For the 3-point function, we use Eq. (8) to obtain the boundary correlators and compare
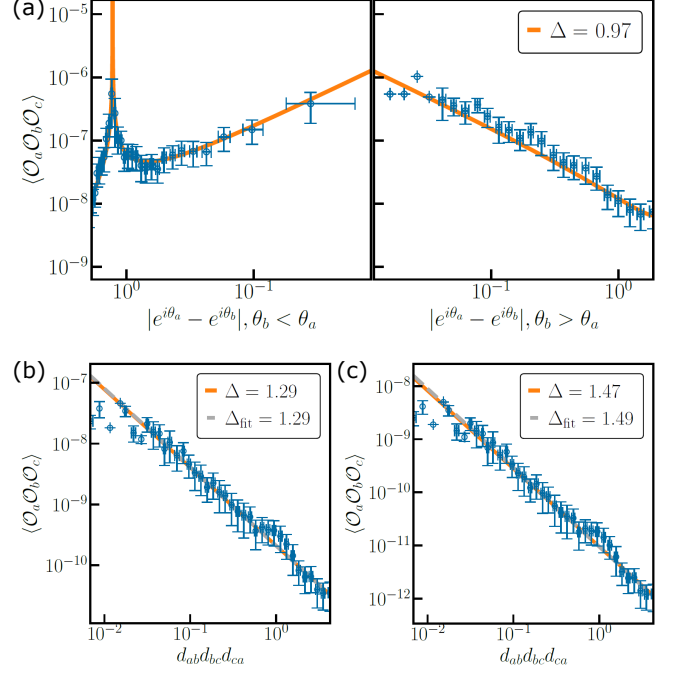
to the zero temperature scaling formula

$$\langle \mathcal{O}_a \mathcal{O}_b \mathcal{O}_c \rangle \simeq \frac{\bar{C}_3}{(d_{ab} d_{ac} d_{bc})^\Delta} \tag{S103}$$

with $d_{ab} = |e^{i\theta_a} - e^{i\theta_b}|$. Similar to the 2-point function, a linear least-square fit of the 3-point function over the product over the three relative distances $d_{ab} d_{ac} d_{bc}$ demonstrates the expected power-law behavior as seen in Fig. 4. In Fig. 4 (b) and (c), a robust evidence for the conformal symmetry emerges as the scaling dimension Δ obtained from the scaling-collapse of the 3-point function for different masses shows good agreement with Δ obtained from the 2-point function. To average out the discreteness of the data, we consider independent sets of 3-point functions with one fixed angle θ_a, and two varying angles θ_b and θ_c, the last of which parametrizes the data sets. A given realization with a fixed set of two angles $\theta_{a,c}$ (Fig. 4 shows an example) contains 3-point function data that is binned and fitted, and the overall scaling dimension is obtained from averaging over the dif-
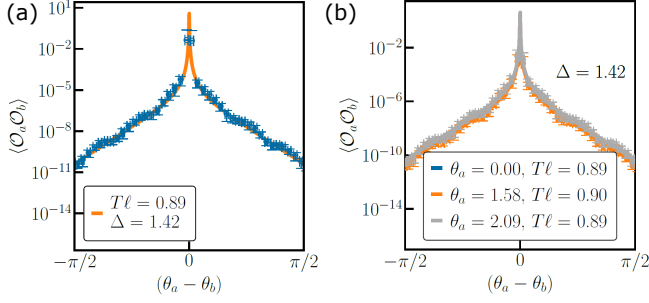
FIG. 5. Thermal boundary 2-point function obtained by applying Eq. (7) for a type-II graph with $k = 12$, obtained by squash-and-wrap from a flake with 6 shells, and bulk scalar mass $m^2\ell^2 = 0.740$. **(a)** The orange fit line is given by Eq. S104 with the sum extending over $n \in [-120, 120]$. In **(d)**, the variation of the 2-point function over a set of varying anchoring coordinates θ_a is shown to lead to only a mild variation of the fitted temperature.

ferent data sets. This yields the comparison between the 2-point and 3-point fits of the scaling dimension shown in Fig 3d in the main text.

Type-II / Finite temperature

2-point functions.—We compute the 2-pt function through Eq. (7) on the type-II flakes for various values of k. To extract the temperature of the boundary CFT, we fit the boundary 2-pt correlator to the continuum limit form

$$\langle \mathcal{O}_a \mathcal{O}_b \rangle = \sum_{n \in \mathbb{Z}} \frac{\bar{C}_2'}{(d_{ab}^{(n)})^{2\Delta}} \qquad \text{(S104)}$$

with

$$d_{ab}^{(n)} = \frac{\sinh(\pi T\ell|\theta_a - \theta_b + 2\pi n|)}{\pi T\ell}. \qquad \text{(S105)}$$

This continuum form is derived from the formula for a constant time-slice of the 3D BTZ black hole geometry. The sum over n is reminiscent of the method of images, and produces a periodic function. We find that the sum converges quickly with $|n| \lesssim 120$ images and yields a very good agreement, see Fig. 5. While the scaling dimension $\Delta(m^2\ell^2)$ can be fitted for the type-II 2-pt function, we find that it is consistent with the type-I result $\Delta(m^2\ell^2)$. For this reason, to increase the accuracy of the temperature fit, we use the relation $\Delta(m^2\ell^2)$ from type-I for the fit of $T\ell$ in Eq. (S104) and confirm the relation $T\ell = kP/8\pi$. The rugged-boundary problem is addressed in the same way as for the type-I graphs discussed above. We average the temperature fits across various θ_a-parametrized data sets, leading to the favorable comparison with the Hawking temperature associated with the BTZ geometry.

3-point functions.—To produce Fig 3b in the main text, we fix $\theta_a = 0$ and θ_c, and vary θ_b. We compare the 3-point function obtained from applying Eq. (8) against the form anticipated for a timeslice of a 3D BTZ black hole given by

$$\langle \mathcal{O}_a \mathcal{O}_b \mathcal{O}_c \rangle = \sum_{n \in \mathbb{Z}} \frac{\bar{C}_3'}{(d_{ab} d_{ac} d_{bc})^\Delta} \bigg|_{\theta_b \to \theta_b + 2\pi n}, \qquad \text{(S106)}$$

$$= \sum_{n \in \mathbb{Z}} \frac{\bar{C}_3'}{(d_{ab}^{(n)} d_{ac} d_{bc}^{(-n)})^\Delta}. \qquad \text{(S107)}$$

The case of various masses is shown in Fig. 8, together with with their scaling collapse.

3-pt coefficient

The normalized 3-point coefficient C_3 is given by

$$C_3 = \frac{\bar{C}_3}{(\bar{C}_2)^{3/2}} \qquad \text{(S108)}$$

in the type-I case, and similarly $C_3 = \bar{C}_3'/(\bar{C}_2')^{3/2}$ in the type-II case. For a systematic way to fit C_3, we construct the ratio

$$F_{abc} = \frac{\langle \mathcal{O}_a \mathcal{O}_b \mathcal{O}_c \rangle}{[\langle \mathcal{O}_a \mathcal{O}_b \rangle \langle \mathcal{O}_a \mathcal{O}_c \rangle \langle \mathcal{O}_b \mathcal{O}_c \rangle]^{1/2}} \qquad \text{(S109)}$$

that we sample over many values of a, b, c. The idea of using F_{abc} is that, naively, one could simply sample

$$\lim_{d_{ab} d_{bc} d_{ca} \to \infty} \langle \mathcal{O}_a \mathcal{O}_b \mathcal{O}_c \rangle (d_{ab} d_{ac} d_{bc})^\Delta \simeq C_3, \qquad \text{(S110)}$$

and determine C_3 from this. However, for the type-II lattices we construct here as described in Sec. S2, the ring boundary is too rough and leads to a k-fold modulation of the 2-pt function already, which amplifies when considering the 3-pt function. (The type-I boundaries are also somewhat rough but less so than the type-II boundaries.) This could be incorporated by appropriate form-factors for both the 2-pt and 3-pt function. By considering F_{abc}, instead, these effects are expected to cancel, and eventually yield a cleaner prediction of the actual physical type system, whose discrete boundary can be made as smooth as possible, in principle. As Fig. 9 shows, F_{abc} only mildly depends on a, b, c and can be used to determine $F_{abc} \simeq C_3$ as long as we stay away from the contact divergences that arise when any two of the boundary sites coincide.

As the comparison in Fig. 10 shows for a fixed $m^2\ell^2$, this approach works satisfactory, with the long-distance asymptotic behavior of F_{abc} yielding an estimate of C_3. We find that C_3 remains consistently close across the type-I and type-II graphs. The coefficient depends on $m^2\ell^2$ and u as depicted in Fig. 3 (e) of the main text.
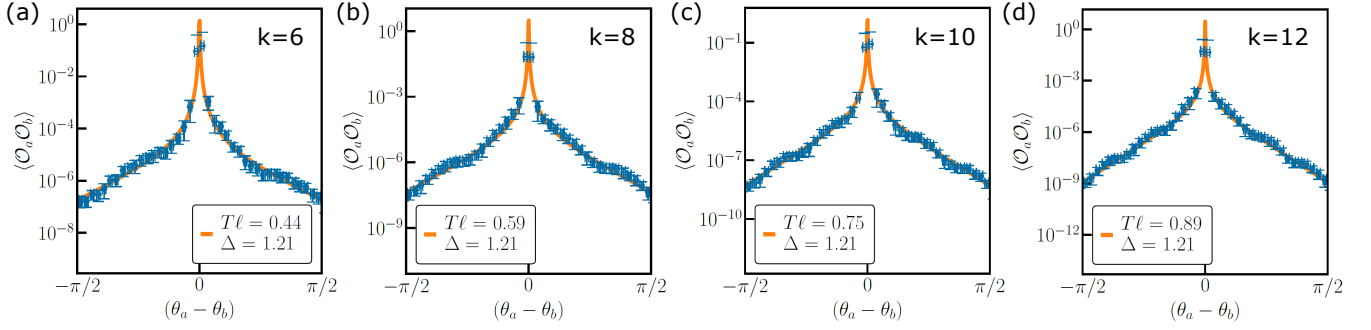
FIG. 6. Type-II 2-point functions for $m^2\ell^2 = 0.32$ shown for (**a**) $k = 6$, (**b**) $k = 8$, (**c**) $k = 10$, and, (**d**) $k = 12$, plotted vs. $\theta_a - \theta_b$ along with orange fit lines from Eq. (S104).
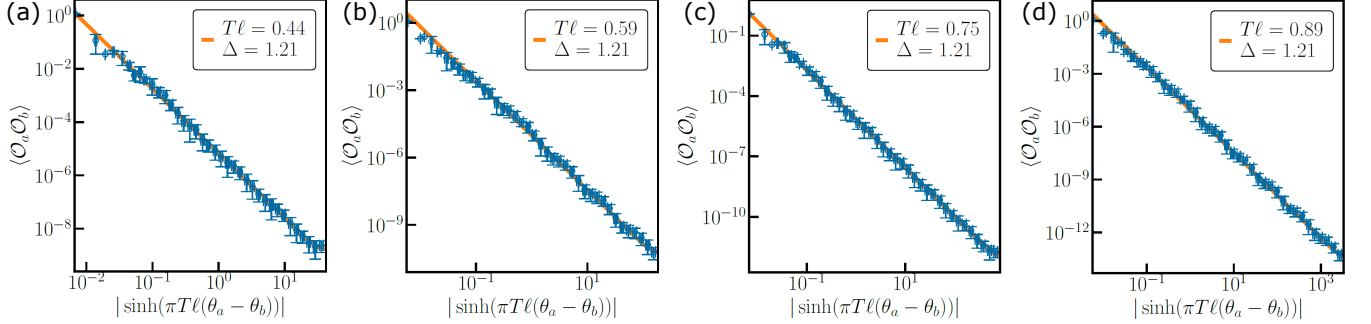

FIG. 7. Type-II 2-point functions for $k = 6, 8, 10,$ and 12 (**(a)-(d)**) as in Fig. 6, plotted vs. $d_{ab}(T)$.

S8. SIMULATION IN ELECTRICAL CIRCUITS

We first describe how to realize the equation of motion (EOM) in Eq. (12) in an electrical circuit network consisting of resistors and diodes. Resistors R_0 are connected between circuit nodes according to the adjacency graph of the respective lattice, resistors $R_{\rm g}$ are connected between each node and ground, and a diode is placed between each node and ground. The resistors correspond to the linear terms of the EOM, whereas the diode introduces the on-site nonlinearity.

The current through a diode is approximately described by the Shockley equation $I(V) = I_{\rm S}(e^{\frac{V}{V_{\rm S}}} - 1)$, which, expanded to second order, reads $I(V) = c_1 V + c_2 V^2 + \mathcal{O}(V^3)$, with c_1, c_2 constants that depend on the specific diode. The values of $\bar{V}_\mu$ are represented by the voltages at the circuit nodes, with $\bar{V}_i$ in the bulk and $\bar{V}_a = J_a$ is realized by applying a fixed voltage at the respective boundary sites. The EOM only needs to be implemented for the bulk sites $\bar{V}_i$. Starting from the general EOM in Eq. (12) for any site μ,

$$\sum_\nu M_{\mu\nu}\bar{V}_\nu + \frac{u}{2}\bar{V}_\mu^2 = 0 \qquad (S111)$$

with $M_{\mu\nu} = -A_{\mu\nu} + \hat{m}^2\delta_{\mu\nu}$, we find

$$\sum_j M_{ij}\bar{V}_j + \frac{u}{2}\bar{V}_i^2 = I_i^{\rm eff} \qquad (S112)$$

for the bulk sites, with an effective bulk source term

$$I_i^{\rm eff} = I_i^{\rm eff}(\{J_a\}) = -\sum_a M_{ia}J_a. \qquad (S113)$$

To derive the EOM of the circuit, we add up all currents flowing out of one node, including up to second order in V_i. According to Kirchhoff's current law, we then obtain

$$I_i = \frac{1}{R_0}\sum_j (q\,\delta_{ij} - A_{ij})\,V_j + \frac{1}{R_{\rm g}}V_i + c_1 V_i + c_2 V_i^2. \qquad (S114)$$

Here, I_i is any external current fed into the circuit nodes, for example from a connected voltage source. If no external supplies are added to a node then $I_i = 0$, while a fixed voltage gives the corresponding current $I_i = I_i^{\rm eff}(\{J_a\})$. Furthermore, in practice (and in numerical simulations), a small parasitic capacitance will be present at each node, contributing an additional term of $C_i\dot{V}_i(t)$. Much like the process of discharging a capacitor, the voltages at the circuit nodes will decay exponentially towards the equilibrium state where $\dot{V}_i = 0$, so that the solution for Eq.
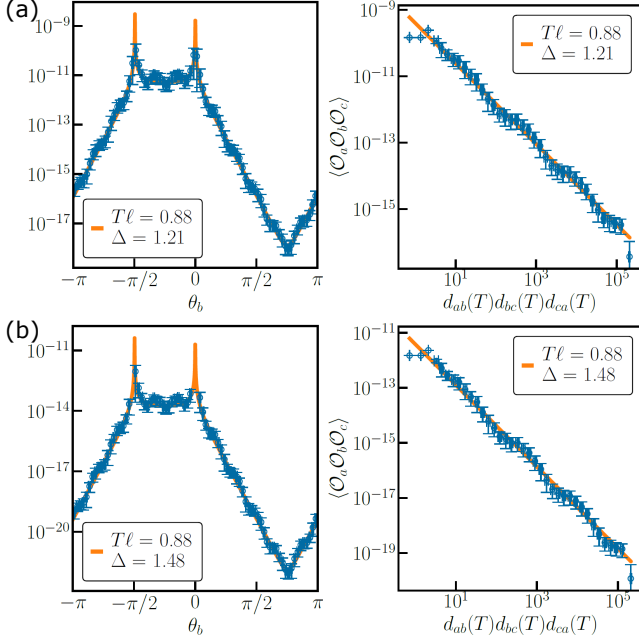
FIG. 8. The 3-point functions at the boundary of the type-II graph with $k = 12$, for $m^2\ell^2 = 0.32$ **(a)** and $m^2\ell^2 = 0.90$ **(b)**. The observed contact divergences (left panels) and asymptotic thermal scaling (right panels) are consistent with the expected conformal behavior.
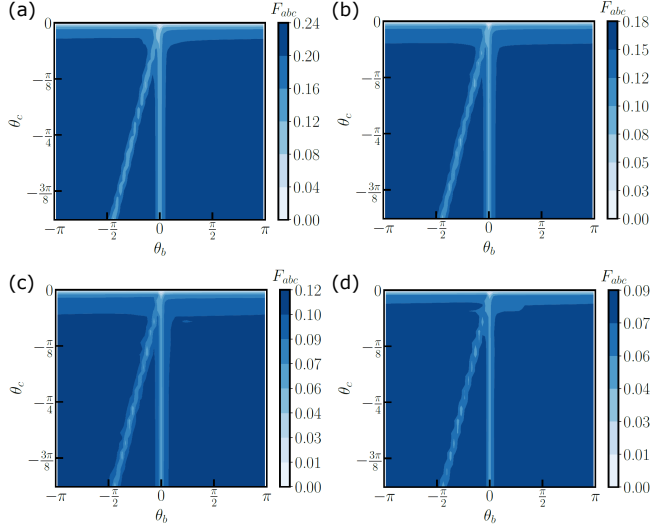

FIG. 9. Normalized 3-point ratio (S109) plotted for fixed $\theta_a = 0$, and varying values of θ_b and θ_c on the boundary of the type-I graph obtained for the bulk scalar mass $m^2\ell^2 = 0.11$ **(a)**, 0.32 **(b)**, 0.63 **(c)**, and 0.95 **(d)**. The value of F_{abc} approaches the saturation value C_3 away from the lines the contact divergences, given by $\theta_c = \theta_a = 0$, $\theta_b = \theta_a = 0$, and $\theta_c = \theta_c$.

FIG. 10. Asymptotic scaling form of the normalized ratio F_{abc} for $m^2\ell^2 = 0.06$ plotted in **(a)** for the type-I boundary at zero-temperature, and for type-II boundary with $k = 4$, $k = 8$, and $k = 10$ **(b)-(d)**. The limit $F_{abc} \simeq C_3$ (left region of the plots where the argument approaches zero) is approximately independent of T, see Fig. 3e in the maintext.

instantaneously.

The relationship between circuit parameters and those of Eq. (12) is found from matching

$$\sum_j (-A_{ij} + \hat{m}^2 \delta_{ij})\bar{\phi}_j + \frac{u}{2}\bar{\phi}_i^2 \tag{S115}$$

$$\stackrel{!}{=} c\left[\frac{1}{R_0}\sum_j (q\,\delta_{ij} - A_{ij})\,V_j + \frac{1}{R_g}V_i + c_1 V_i + c_2 V_i^2\right]. \tag{S116}$$

Here, $c = R_0/V_0$ is an arbitrary proportionality constant, and V_0 is a voltage scale that can be chosen freely (we set $V_0 = 1$ in the main text for simplicity). The matching yields the values shown this table:

$\bar{\phi}_\mu$	$\hat{m}^2$	$u/2$
V_μ/V_0	$q + R_0(R_g^{-1} + c_1)$	$V_0 R_0 c_2$

We chose a Schottky diode (model RBE1VAM20A) for its low threshold voltage and high switching speed. From a calibration fit of the diode we extract the parameters $c_1 = 5.24 \cdot 10^{-4}$ and $c_2 = 9.43 \cdot 10^{-3}$. After arbitrarily fixing $R_0 = 100\Omega$, we choose $R_g = 240.3\Omega$ in order to obtain the target value of $m^2\ell^2 = \frac{1}{qh^2}R_0(R_g^{-1} + c_1) = 0.271$, which is the mass used in Figs. 2 and 3 in the maintext. These parameters correspond to a non-linearity coefficient $u/2 = 0.943V_0$.

(12) is obtained as $t \to \infty$. In the following, we assume that all parasitic capacitances are so small that the equilibrium (or a sufficient approximation thereof) is reached
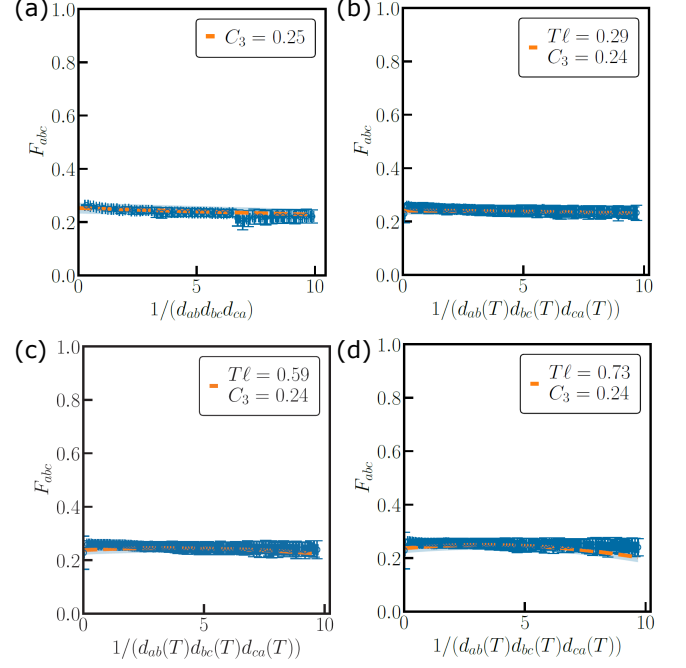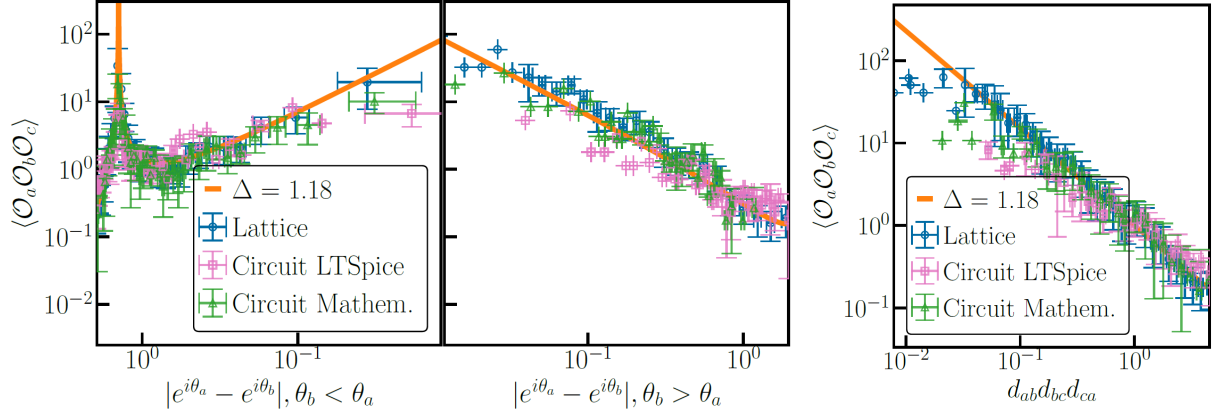
FIG. 11. Comparison of circuit simulation using Mathematica (green) and LTspice (pink) for a small flake. For larger flakes with more sites, as presented in Fig. 3b of the main text, the LTspice simulation becomes noisier or larger distances, while the Mathematica simulation is still reliable. Note that the circuit data is normalized differently (choice of C_3) compared to Fig. 3b to make both data sets agree better for small distances.

The linear-ramp protocol to compute $W_{\mathrm{circ}}(t)$ is implemented in the analog electronic circuit simulator computer software LTspice for each set(a, b) and (a, b, c) for the 2-pt and 3-pt correlation functions, respectively. The generating function of each run $W_{\mathrm{circ}}(t)$ is exported to a Mathematica notebook where the corresponding linear system is solved giving the correlation functions. For the 3-pt function, while the LTspice simulation works in practice, we use Mathematica to simulate the circuit EOM directly to reduce noise of the data. A comparison for small flakes, where the deviations are smaller, is shown in Fig. 11.

* santanu@ualberta.ca
† anffany@ualberta.ca

[1] P. Ginsparg and G. Moore, Lectures on 2D gravity and 2D string theory (TASI 1992), hep-th/9304011 (1993).

[2] I. Boettcher, P. Bienias, R. Belyansky, A. J. Kollár, and A. V. Gorshkov, Quantum simulation of hyperbolic space with circuit quantum electrodynamics: From graphs to geometry, Phys. Rev. A **102**, 032208 (2020).

[3] L. Boyle, M. Dickens, and F. Flicker, Conformal Quasicrystals and Holography, Phys. Rev. X **10**, 011009 (2020).

[4] A. Jahn, Z. Zimborás, and J. Eisert, Central charges of aperiodic holographic tensor-network models, Phys. Rev. A **102**, 042407 (2020).

[5] A. Chen, Y. Guan, P. M. Lenggenhager, J. Maciejko, I. Boettcher, and T. Bzdušek, Symmetry and topology of hyperbolic Haldane models, Phys. Rev. B **108**, 085114 (2023).

[6] S. Carlip and C. Teitelboim, Aspects of black hole quantum mechanics and thermodynamics in 2+1 dimensions, Phys. Rev. D **51**, 622 (1995).

[7] M. Ammon and J. Erdmenger, Gauge/gravity duality: Foundations and applications (Cambridge University Press, Cambridge, 2015).

[8] A. Stegmaier, L. K. Upreti, R. Thomale, and I. Boettcher, Universality of Hofstadter Butterflies on Hyperbolic Lattices, Phys. Rev. Lett. **128**, 166402 (2022).